NEAR-INFRARED INTERFEROMETRIC MEASUREMENTS OF HERBIG Ae/Be STARS

J. A. EISNER,[1] B. F. LANE,[2] R. L. AKESON,[3] L. A. HILLENBRAND,[1] AND A. I. SARGENT[1]

ABSTRACT

We have observed the Herbig Ae/Be sources AB Aur, VV Ser, V1685 Cyg (BD +40°4124), AS 442, and MWC 1080 with the Palomar Testbed Interferometer, obtaining the longest baseline near-IR interferometric observations of this class of objects. All of the sources are resolved at 2.2 μm with angular size scales generally $\lesssim 5$ mas, consistent with the only previous near-IR interferometric measurements of Herbig Ae/Be stars, by Millan-Gabet and collaborators. We determine the angular size scales and orientations predicted by uniform-disk, Gaussian, ring, and accretion disk models. Although it is difficult to distinguish different radial distributions, we are able to place firm constraints on the inclinations of these models, and our measurements are the first that show evidence for significantly inclined morphologies. In addition, the derived angular sizes for the early-type Herbig Be stars in our sample, V1685 Cyg and MWC 1080, agree reasonably well with those predicted by the face-on accretion disk models used by Hillenbrand and collaborators to explain observed spectral energy distributions. In contrast, our data for the later-type sources AB Aur, VV Ser, and AS 442 are somewhat inconsistent with these models and may be explained better through the puffed-up inner disk models of Dullemond and collaborators.

Subject headings: infrared: stars — stars: emission-line, Be —
stars: individual (AB Aurigae, AS 442, MWC 1080, V1685 Cygni, VV Serpentis) —
stars: pre–main-sequence — techniques: high angular resolution

1. INTRODUCTION

Herbig Ae/Be (HAEBE) stars (Herbig 1960) are intermediate-mass (2–10 $M_\odot$), young stellar objects that show broad emission lines, rapid variability, and excess infrared and millimeter-wavelength emission. These properties are consistent with the presence of hot and cold circumstellar dust and gas. While there is still some debate about the morphology of this circumstellar material, most evidence supports the hypothesis that in many cases the dust and gas lie in a massive (~ 0.01 $M_\odot$) circumstellar disk (Natta, Grinin, & Mannings 2000; Hillenbrand et al. 1992, hereafter HSVK).

The strongest evidence for circumstellar disks around HAEBE stars comes from direct imaging with millimeter interferometry. Flattened structures around several sources have been resolved on ~ 100 AU scales (Mannings & Sargent 1997, 2000; Piétu, Dutrey, & Kahane 2003), and detailed kinematic modeling of one source, MWC 480, shows that the observations are well fitted by a rotating Keplerian disk (Mannings, Koerner, & Sargent 1997). For a spherical distribution, these and other observations (see, e.g., Mannings 1994) imply extinctions at visible and infrared wavelengths much higher than actually observed. In addition, in recent Hα spectropolarimetric observations of HAEBE sources (which trace dust on scales of tens of stellar radii), Vink et al. (2002) find signatures of flattened circumstellar structures around 83% of their sample and evidence for rotation around nine HAe stars. Furthermore, the

forbidden emission lines that arise in winds and outflows around HAEBE sources typically show blueshifted emission but lack redshifted emission, which suggests that the redshifted component of the outflow is occluded by a circumstellar disk. The broad line widths of low-velocity features are consistent with this emission arising in rotating circumstellar disk winds (Corcoran & Ray 1997).

The distribution of circumstellar material around HAEBE stars can also be inferred from modeling of spectral energy distributions (SEDs). Three distinct morphologies were identified in this way by HSVK, who classified observed HAEBE sources into three groups, I, II, and III. All sources in our observed sample fall into group I, which has SEDs of the form $\lambda F_\lambda \propto \lambda^{4/3}$. These can be modeled well by flat, irradiated, accretion disks with inner holes on the order of ~ 10 stellar radii. Recent SED modeling of a sample of 14 isolated HAEBE stars with the characteristics of group I sources is consistent with emission from a passive reprocessing disk (Meeus et al. 2001). Moreover, Meeus et al. (2001; and other investigators; e.g., Natta et al. 2001) attribute this emission to the outer part of a flared circumstellar disk (see, e.g., Chiang & Goldreich 1997), while previous authors attributed blackbody components observed in SEDs of HAEBE sources to tenuous envelopes (Hartmann, Kenyon, & Calvet 1993; Miroshnichenko et al. 1999; Natta et al. 1993).

Size scales and orientations of disks around HAEBE stars can only be determined directly through high angular resolution imaging. The spatial and velocity structure of cooler outer HAEBE disks on ~ 100 AU scales has been mapped with millimeter-wavelength interferometers (as discussed above). To probe the warmer inner regions of the disk (~ 1 AU scales), measurements with near-IR interferometers are necessary. The only near-IR interferometric observations of HAEBE sources to date, conducted with the IOTA interferometer (Millan-Gabet et al. 1999; Millan-Gabet,

[1] Department of Astronomy, California Institute of Technology, MC 105-24, Pasadena, CA 91125; jae@astro.caltech.edu.

[2] Department of Geological and Planetary Sciences, California Institute of Technology, MC 150-21, Pasadena, CA 91125.

[3] Michelson Science Center, California Institute of Technology, MC 100-22, Pasadena, CA 91125.

Schloerb, & Traub 2001, hereafter MST), led to sizes and orientations of sources largely inconsistent with values estimated using other techniques. A geometrically flat disk may be too simplistic to accommodate all the observations, and puffed-up inner disk walls (Dullemond, Dominik, & Natta 2001, hereafter DDN) or flared outer disks (see, e.g., Chiang & Goldreich 1997) may need to be included in the models. However, the limited number of HAEBE sources observed with near-IR interferometers and the sparse u-v coverage of these observations (MST) make it difficult to draw unambiguous conclusions about the structure of the circumstellar material.

We have begun a program with the Palomar Testbed Interferometer (PTI) to observe HAEBE stars. By increasing the sample size and improving u-v coverage, we aim to understand better the structure of the circumstellar emission on ~1 AU scales. In this paper, we present results for five sources, AB Aur, VV Ser, V1685 Cyg (BD +40°4124), AS 442, and MWC 1080. We note that neither our list of HAEBE stars nor that of MST represents an unbiased sample but rather they are limited to those stars that are bright enough ($K \lesssim 6.5$) to be successfully observed. We model the structure of circumstellar dust around HAEBE stars using these PTI data, together with IOTA measurements where available. Specifically, we compare various models—Gaussians, uniform disks, uniform rings, and accretion disks with inner holes—to the visibility data to determine approximate size scales and orientations of the circumstellar emission.

In § 2, we describe the PTI observations. In § 3, we fit the observed data to several different models for the circumstellar dust distribution and derive angular sizes and orientations. Implications of the modeling and comparisons with previous observations are discussed in § 4.

2. OBSERVATIONS AND CALIBRATION

The PTI is a long-baseline, near-IR Michelson interferometer located on Palomar Mountain near San Diego, California (Colavita et al. 1999). The PTI combines starlight from two 40 cm aperture telescopes using a Michelson beam combiner and records the resulting fringe visibilities. These fringe visibilities are related to the source brightness distribution via the van Cittert–Zernike theorem, which states that the visibility distribution in u-v space and the brightness distribution on the sky are Fourier transform pairs (Born & Wolf 1999).

We observed five HAEBE sources, AB Aur, VV Ser, V1685 Cyg (BD +40°4124), AS 442, and MWC 1080, with PTI between 2002 May and October. Properties of the sample are included in Table 1. We obtained K-band (2.2 μm) measurements on an 85 m northwest baseline for all five objects and on a 110 m north-south baseline for three. The northwest baseline is oriented 109° west of north and has a fringe spacing of ~5 mas, and the north-south baseline is 160° west of north and has a fringe spacing of ~4 mas. A summary of the observations is given in Table 2.

PTI measures fringes in two channels, corresponding to the two outputs from the beam combiner. One output is spatially filtered with an optical fiber and dispersed onto five "spectral" pixels, while the other output is focused onto a single "white-light" pixel (without spatial filtering). The white-light pixel is used principally for fringe tracking: the fringe phase is measured and then used to control the delay line system to track atmospheric fringe motion (and thus maintain zero optical path difference between the two interfering beams). The spectral pixels are generally used to make accurate measurements of the squared visibility amplitudes (V^2) of observed sources. We sample the data at either 20 or 50 ms in order to make measurements on a timescale shorter than the atmospheric coherence time. A "scan," which is the unit of data we use in the analysis below, consists of 130 s of data, divided into five equal time blocks. The V^2 is calculated for each of these blocks using an incoherent average of the constituent 20 or 50 ms measurements from a synthetic wide-band channel formed from the five spectral pixels (Colavita 1999). V^2 for the entire scan is given by the mean of these five estimates, and the statistical uncertainty is given by the standard deviation from the mean value.

We calibrate the measured V^2 for the observed HAEBE sources by comparing them to visibilities measured for calibrator sources of known angular sizes, for which we can easily calculate the expected V^2 for an ideal system. The visibilities are normalized such that $V^2 = 1$ for a point source observed with an ideal system. We calculate the expected V^2 by assuming that the calibrators are uniform stellar disks. Making use of the van Cittert–Zernike theorem, the squared visibilities for these sources are given by

$$V_{\rm calc}^2 = \left[2 \frac{J_1(\pi \theta r_{u\text{-}v})}{\pi \theta r_{u\text{-}v}} \right]^2 . \tag{1}$$

Here, J_1 is the first-order Bessel function, θ is the angular

TABLE 1
Observed Sources

Source	Alternate Name	α (J2000.0)	δ (J2000.0)	d (pc)	Spectral Type	V	K	F_*[a] (Jy)	F_x[a] (Jy)
AB Aur	HD 31293	04 55 45.84	+30 33 04.3	140	A0 pe	7.07	4.27	1.92	10.59
VV Ser	HBC 282	18 28 49.00	+00 08 39.0	310	A0 Vevp	11.90	6.44	0.20	1.85
V1685 Cyg	BD +40°4124	20 20 28.25	+41 21 51.6	1000	B2 Ve	10.71	5.70	0.42	3.64
AS 442	V1977 Cyg	20 47 37.47	+43 47 24.9	600	B8Ve	10.89	6.75	0.20	1.21
MWC 1080	V628 Cas	23 17 26.10	+60 50 43.0	1000	B0 eq	11.68	4.83	0.87	9.85

NOTE.—Units of right ascension are hours, minutes, and seconds, and units of declination are degrees, arcminutes, and arcseconds. Distances, spectral types, and V magnitudes are from HSVK, Mora et al. 2001, Strom et al. 1972, de Lara et al. 1991, and Bigay & Garner 1970. For a discussion of the adopted distances, see the Appendix. K magnitudes are from the present work.

[a] Dereddened fluxes.

TABLE 2
SUMMARY OF OBSERVATIONS

Source	Date (MJD)	Baseline	Hour Angle Coverage	Calibrators (HD)
AB Aur	52,575	NW	[1.21, 1.85]	29645, 32301
	52,602	NW	[−1.95, 1.51]	29645, 32301
VV Ser	52,490	NW	[−0.72, 0.54]	171834
	52,491	NS	[−1.55, −0.74]	171834
	52,493	NW	[−1.31, 0.20]	171834
	52,499	NW	[−0.96, 0.84]	164259, 171834
V1685 Cyg	52,418	NW	[−1.10, −1.00]	192640, 192985
	52,475	NW	[−1.69, 1.44]	192640, 192985
	52,476	NW	[−1.80, −0.48]	192640, 192985
	52,490	NW	[−0.97, 1.70]	192640, 192985
	52,491	NS	[−1.27, 2.38]	192640
	52,492	NW	[−0.90, −0.90]	192640
	52,545	NS	[−1.12, 2.48]	192640, 192985
AS 442	52,475	NW	[0.21, 1.33]	192640, 192985
	52,476	NW	[−0.21, −0.21]	192640, 192985
	52,490	NW	[−1.11, 0.38]	192640
	52,491	NS	[−0.69, 2.54]	192640
	52,492	NW	[−1.05, 0.00]	192640
	52,545	NS	[−0.87, 1.58]	192640, 192985
MWC 1080	52,475	NW	[0.17, 0.17]	219623
	52,476	NW	[−1.99, 0.52]	219623
	52,490	NW	[−0.14, 1.39]	219623

diameter of the star, and $r_{u\text{-}v}$ is the "$u\text{-}v$ radius," defined by

$$r_{u\text{-}v} = \sqrt{u^2 + v^2} = \frac{\boldsymbol{B} \cdot \boldsymbol{s}}{\lambda} , \qquad (2)$$

where $\boldsymbol{B}$ is the baseline vector, $\boldsymbol{s}$ is a unit vector pointing from the center of the baseline toward the source, and λ is the observing wavelength. (The qualitative explanation of eq. [1] is that while for unresolved sources the visibility is constant with increasing $u\text{-}v$ radius, for progressively larger sources, the visibility decreases faster with increasing $u\text{-}v$ radius.) By comparing V^2_{calc} to the measured V^2 for a calibrator, we derive the "system visibility," which represents the point-source response of the interferometer:

$$V^2_{\text{sys}} = \frac{V^2_{\text{meas,calibrator}}}{V^2_{\text{calc}}} . \qquad (3)$$

This system visibility, in turn, is used to calibrate the squared visibilities for the target source:

$$V^2_{\text{target}} = \frac{V^2_{\text{meas,target}}}{V^2_{\text{sys}}} . \qquad (4)$$

Specifically, we determine V^2_{sys} at the time of each target scan, using an average of $V^2_{\text{meas,calibrator}}$ weighted by the proximity of the target and calibrator in both time and angle. For further discussion of the calibration procedure, see Boden et al. (1998).

Calibrators must be close to the target sources (on the sky and in time) so that the atmospheric effects will be the same for both. They should also be of small angular size, θ, so that $V^2 \to 1$ and $dV^2_{\text{sys}}/d\theta \to 0$, and the calibration is thus less sensitive to uncertainties in the assumed calibrator diameter. The angular size of a calibrator can be estimated from the published stellar luminosity and distance, from a blackbody fit to published photometric data with the

temperature constrained to that expected for the published spectral type, or from an unconstrained blackbody fit to the photometric data. We adopt the average of these three size estimates in our analysis, and the uncertainty is given by the spread of these values. Relevant properties of the calibrators used in these observations are given in Table 3.

3. RESULTS

We measured calibrated squared visibilities for AB Aur, VV Ser, V1685 Cyg, AS 442, and MWC 1080 (Table 2). All five sources are resolved by PTI (i.e., V^2 is significantly different from unity), implying angular sizes $\gtrsim 1$ mas. The data are consistent with disklike morphologies for all sources, and we can place good constraints on disk inclinations for most sources. MWC 1080, V1685 Cyg, and VV Ser show evidence for significantly nonzero inclinations, while a circularly symmetric distribution appears appropriate for AB Aur. The AS 442 data are insufficient to constrain the inclination.

Interferometric observations of AB Aur and MWC 1080 at 2.2 μm have also been obtained with the 21 and 38 m baselines of the IOTA interferometer (Millan-Gabet et al. 1999; MST). When combined with our longer baseline PTI data (85 and 110 m), these help fill in the $u\text{-}v$ plane and enable us to improve constraints on source models (see Fig. 1). Based on discussion with R. Millan-Gabet, we assign an uncertainty to each IOTA visibility given by the standard deviation of all data obtained for a given source with a given baseline. We verify the registration of the IOTA and PTI data using calibrators observed by both interferometers. Since the IOTA data for AB Aur were calibrated using HD 32406, which is unresolved by both PTI and IOTA, we can be confident of the registration. We measured the diameter of HD 220074, the calibrator for MWC 1080, to be $\theta_{\text{UD}} = 1.98 \pm 0.06$ mas, while MST assumed a size of

TABLE 3
Properties of Calibrator Sources

Name	α (J2000.0)	δ (J2000.0)	Spectral Type	V	K	Calibrator Size (mas)	$\Delta\alpha$ (deg)
HD 29645	04 41 50.26	+38 16 48.7	G0 V	6.0	4.6	0.56 ± 0.09	8.2
HD 32301	05 03 05.75	+21 35 23.9	A7 V	4.6	4.1	0.47 ± 0.10	9.1
HD 164259..............	18 00 29.01	−03 41 25.0	F2 IV	4.6	3.7	0.77 ± 0.08	7.5
HD 171834..............	18 36 39.08	+06 40 18.5	F3 V	5.4	4.5	0.54 ± 0.07	6.8
HD 192640..............	20 14 32.03	+36 48 22.7	A2 V	4.9	4.9	0.46 ± 0.02	4.7,[a] 9.4[b]
HD 192985..............	20 16 00.62	+45 34 46.3	F5 V	5.9	4.8	0.44 ± 0.04	4.3,[a] 5.9[b]
HD 219623..............	23 16 42.30	+53 12 48.5	F7 V	5.6	4.3	0.54 ± 0.03	9.5

Note.—Units of right ascension are hours, minutes, and seconds, and units of declination are degrees, arcminutes, and arcseconds.

[a] Offset from V1685 Cyg.

[b] Offset from AS 442.

2.10 ± 0.22 mas. This difference in angular size translates into only a 0.7% effect, which is within the measurement errors (the effect is so small because the calibrator is essentially unresolved by IOTA).

3.1. Visibility Corrections

Nearby companions that lie outside the interferometric field of view, ∼50 mas, but within the field of view of the detector, ∼1″, will contribute incoherent light to the visibilities. For MWC 1080, which has a known nearby companion (Corporon 1998), we use the correction factor

$$\frac{V_{\text{true}}^2}{V_{\text{meas}}^2} = \left(\frac{1}{1 + 10^{\Delta K/2.5}}\right)^2, \qquad (5)$$

where ΔK is the difference in K-band magnitudes between the two stars. For MWC 1080, we measured $\Delta K = 2.70$ (angular separation = 0″78) using the Palomar Adaptive Optics system on the 200 inch (5.08 m) telescope on 2002 November 18. V1685 Cyg is also known to have a faint companion ($\Delta K = 5.50$; Corporon 1998), but the effect of this companion on the visibilities is negligible. Adaptive optics images of the other sources in our sample show that none of these have any bright companions ($\Delta K < 5$) at distances between ∼50 mas and 1″.

Our measured visibilities contain information about emission from both the circumstellar material and the star itself. We can remove the effect of the central star on the visibilities by including it in the models:

$$V_{\text{tot}}^2 = \left(\frac{F_* V_* + F_x V_x}{F_* + F_x}\right)^2 \approx \left(\frac{F_* + F_x V_x}{F_* + F_x}\right)^2, \qquad (6)$$

where F_* is the stellar flux, F_x is the excess flux (both measured at 2.2 μm), $V_* \approx 1$ is the visibility of the (unresolved) central star, and V_x is the visibility due to the circumstellar component. It is reasonable to assume that $V_* \approx 1$, since for typical stellar radii (∼5 $R_\odot$) and distances (∼500 pc), the angular diameters of the central stars will be ∼0.5 mas. In the case of the binary model described below (§ 3.3.5), we do not perform any such correction, since the basic model already includes the stellar component.

Equation (6) assumes that the central star is a point source and thus contributes coherently to the visibilities. It is also possible that the starlight is actually observable only

as scattered-light emission and that it will have some incoherent contribution to the visibility ($V_* \neq 1$). For example, coronographic imaging with the Hubble Space Telescope has revealed scattered light on angular scales from ∼0″1 to 9″ around AB Aur (Grady et al. 1999). A proper treatment of the effects of this scattered light on the visibilities is beyond the scope of this work, but we mention it as a possible source of uncertainty. Since the near-IR excess from HAEBE sources typically dominates over the near-IR stellar emission (§ 3.2; Table 1), the effect should be insignificant.

3.2. Photometry

F_* and F_x affect the visibilities (eq. [6]), and thus it is important to determine these quantities accurately. Since HAEBE objects are often highly variable at near-IR wavelengths (see, e.g., Skrutskie et al. 1996), we obtained photometric K-band measurements of the sources in our sample that are nearly contemporaneous with our PTI observations, using the Palomar 200 inch telescope between 2002 November 14 and 18. Calibration relied on observations of 2MASS sources close in angle to the target sources, and we estimate uncertainties of ∼0.1 mag. Our photometry is consistent with published measurements to within ∼0.3 mag for all objects (HSVK; Eiroa et al. 2002).

Following HSVK and MST, we calculate F_* and F_x using our K-band photometry (Table 1) combined with $BVRI$ photometry, visual extinctions, and stellar effective temperatures from the literature (HSVK; Oudmaijer et al. 2001; Eiroa et al. 2002; Bigay & Garnier 1970). Dereddening uses the extinction law of Steenman & Thé (1991). Assuming that all of the short-wavelength flux is due to the central star, we fit a blackbody at the assumed effective temperature to the dereddened BVRI data. The K-band stellar flux is derived from the value of this blackbody curve at 2.2 μm. The excess flux is then given by the difference between the dereddened observed flux and the stellar flux. The derived fluxes are given in Table 1. We note that VV Ser and AS 442 are optically variable by $\Delta V \gtrsim 1$ mag on timescales of days to months (while the other sources in our sample show little or no optical variability; Herbst & Shevchenko 1999), and thus F_* is somewhat uncertain. However, since $F_x/F_* \gg 1$ for these objects, this uncertainty is negligible when modeling the visibilities.
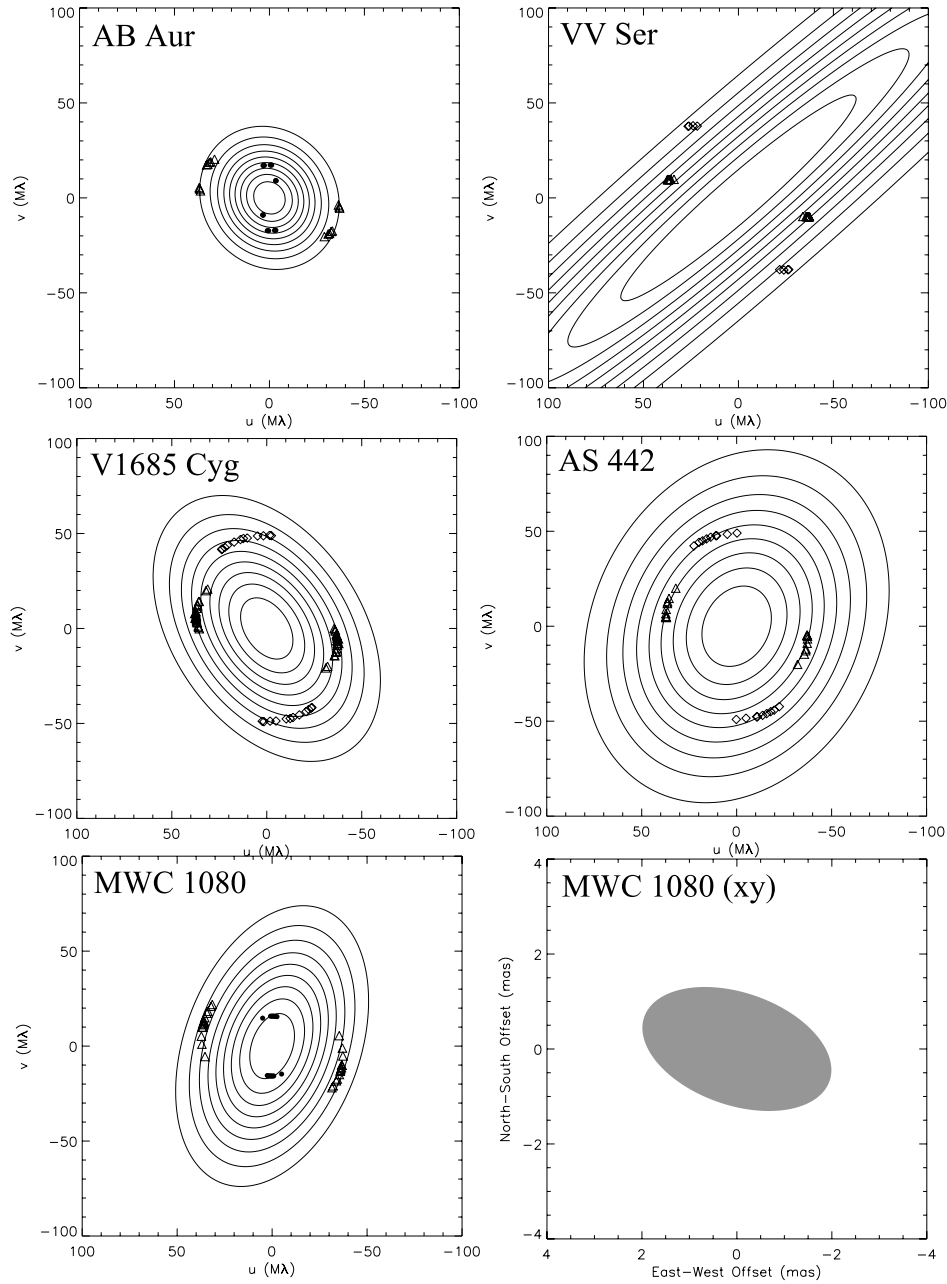
Fig. 1.—Contour plots of best-fit inclined uniform-disk models for AB Aur, VV Ser, V1685 Cyg, AS 442, and MWC 1080, whose parameters are listed in Tables 4–8. The contour increment is 10% in V^2. We also plot the best-fit inclined disk model for MWC 1080 on the sky (*bottom right-hand panel, gray scale*). We overplot the u-v points sampled for each source by the PTI northwest baseline (*triangles*), the PTI NS baseline (*diamonds*), and by IOTA (*filled circles*). Since we know that the brightness distributions of the sources are real, the visibilities must be reflection symmetric (through the origin), and so we also plot these reflections of the sampled u-v points.

3.3. Models

For each source, we compare the observed visibilities to those derived from a uniform-disk model, a Gaussian model, a ring model, and an accretion disk model with an inner disk hole (all models are two-dimensional).

If we assume that the inclination of the circumstellar material is zero, then the one remaining free parameter in the models is the angular size scale θ. When we include inclination effects, we fit for three parameters: size (θ), inclination angle (ϕ), and position angle (ψ). Inclination is defined such that a face-on disk has $\phi = 0$, and ψ is measured east of north. Following MST, we include ϕ and

ψ in our models of the brightness distribution via a simple coordinate transformation:

$$x' = x \sin \psi + y \cos \psi ; \quad y' = \frac{y \cos \psi - x \sin \psi}{\cos \phi} . \quad (7)$$

Here (x, y) are the coordinates on the sky and (x', y') are the transformed coordinates. The effect of this coordinate transformation on the visibilities will be to transform (u, v) to (u', v'):

$$u' = u \sin \psi + v \cos \psi ; \quad v' = \cos \phi (v \sin \psi - u \cos \psi) . \quad (8)$$

Substitution of (x', y') for (x, y) and (u', v') for (u, v) in the

expressions below yields models with inclination effects included.

In addition to these four models, we also examine whether the data are consistent with a wide binary model, which we approximate with two stationary point sources. For this model, the free parameters are the angular separation (θ), the position angle (ψ), and the brightness ratio of the two components (R).

3.3.1. *Gaussian Model*

The brightness distribution for a normalized Gaussian model is given by

$$I_{\mathrm{Gauss}}(x,\ y) = \exp\left[-\frac{4\ln 2(x^2 + y^2)}{\theta^2}\right], \qquad (9)$$

and the (normalized) visibilities expected for this observed brightness distribution are calculated via a Fourier transform to be

$$V_{\mathrm{Gauss}}(r_{u\text{-}v}) = \exp\left(-\frac{\pi^2\theta^2 r_{u\text{-}v}^2}{4\ln 2}\right). \qquad (10)$$

Here (x, y) are the angular offsets from the central star, θ is the angular FWHM of the brightness distribution, and $r_{u\text{-}v} = (u^2 + v^2)^{1/2}$ is the u-v radius (eq. [2]). The model for the observed squared visibilities is obtained by using equation (6) with $V_x = V_{\mathrm{Gauss}}$.

3.3.2. *Uniform-Disk Model*

The brightness distribution for a uniform disk is simply given by a two-dimensional top-hat function. Thus, the normalized visibilities are given by

$$V_{\mathrm{uniform}}(r_{u\text{-}v}) = 2\frac{J_1(\pi\theta r_{u\text{-}v})}{\pi\theta r_{u\text{-}v}}, \qquad (11)$$

where θ is the angular diameter of the uniform-disk brightness distribution and $r_{u\text{-}v} = (u^2 + v^2)^{1/2}$ is the u-v radius (eq. [2]). The model for the observed squared visibilities is obtained by using equation (6) with $V_x = V_{\mathrm{uniform}}$.

3.3.3. *Accretion Disk Model*

We derive the brightness distribution and predicted visibilities for a geometrically thin irradiated accretion disk following the analysis of HSVK and MST. Assuming that the disk is heated by stellar radiation and accretion (Lynden-Bell & Pringle 1974), the temperature profile (in the regime where $R_*/R \ll 1$) is

$$T_{\mathrm{disk}} = T_{1\,\mathrm{AU}}\left(\frac{R}{\mathrm{AU}}\right)^{-3/4}, \qquad (12)$$

where $T_{1\,\mathrm{AU}}$ is defined as the temperature at 1 AU, given by

$$T_{1\,\mathrm{AU}} = \left[2.52 \times 10^{-8}\left(\frac{R_*}{R_\odot}\right)^3 T_*^4\right.$$
$$\left. + 5.27 \times 10^{10}\left(\frac{M_*}{M_\odot}\right)\left(\frac{\dot{M}}{10^{-5}\,M_\odot\,\mathrm{yr}^{-1}}\right)\right]^{1/4}. \qquad (13)$$

We assume that the disk is truncated at an inner radius R_{in} and an outer radius R_{out}. Guided by Figure 14 of HSVK, we choose R_{in} to be the radius at which the temperature, T_{in}, is

2000 K. Thus,

$$T_{1\,\mathrm{AU}} = 2000\left(\frac{R_{\mathrm{in}}}{\mathrm{AU}}\right)^{3/4}. \qquad (14)$$

The value 2000 K is a likely (upper limit) sublimation temperature for the dust grains that make up circumstellar disks, and thus it is reasonable that there would be little or no dust emission interior to R_{in} (although the model does not exclude the possibility of optically thin gas interior to R_{in}). We choose R_{out} to be the lesser of 1000 AU or the radius at which $T = 3$ K (R_{out} is not crucial in this analysis, since most of the near-IR flux comes from the hotter inner regions of the disk).

The brightness distribution and visibilities for this disk are calculated by determining the contributions from a series of annuli from R_{in} to R_{out}. The flux in an annulus specified by inner boundary R_i and outer boundary R_o is given by

$$F_{\mathrm{annulus}} = \frac{\pi}{2d^2}[B_\nu(T_i) + B_\nu(T_o)](R_o^2 - R_i^2), \qquad (15)$$

and the visibilities for this annulus are (following MST)

$$V_{\mathrm{annulus}} = \frac{\pi}{d^2}[B_\nu(T_i) + B_\nu(T_o)]$$
$$\times \left[R_o^2\frac{J_1(\pi\theta_o r_{u\text{-}v})}{\pi\theta_o r_{u\text{-}v}} - R_i^2\frac{J_1(\pi\theta_i r_{u\text{-}v})}{\pi\theta_i r_{u\text{-}v}}\right]. \qquad (16)$$

Here, d is the distance to the source, ν is the observed frequency, B_ν is the Planck function, T is the temperature, R is the physical radius, θ is the angular size, r_{uv} is the u-v radius (eq. [2]), and i, o indicate the inner and outer boundaries of the annulus, respectively. To obtain the visibilities for the entire disk, we sum the visibilities for each annulus, and normalize by the total flux:

$$V_{\mathrm{disk}} = \frac{\sum_{R_{\mathrm{in}}}^{R_{\mathrm{out}}} V_{\mathrm{annulus}}}{\sum_{R_{\mathrm{in}}}^{R_{\mathrm{out}}} F_{\mathrm{annulus}}}. \qquad (17)$$

The resultant model visibilities are obtained by plugging this expression into equation (6). We note that although we do not use the observed excess K-band flux to constrain the disk model, we do verify that the total flux in the model is consistent (to within a factor of 2) with the observations.

3.3.4. *Ring Model*

The brightness distribution for a uniform ring model is given by

$$I_{\mathrm{ring}}(x,\ y) = \begin{cases} \mathrm{constant}, & \mathrm{if}\ \dfrac{\theta_{\mathrm{in}}}{2} < \sqrt{x^2 + y^2} < \dfrac{\theta_{\mathrm{out}}}{2} \\ 0, & \mathrm{otherwise} \end{cases} \qquad (18)$$

Here (x, y) are the angular offsets from the central star. We define the width of the ring via the relation $f = W/R$, where R is the radius of the inner edge of the ring and W is the width of the ring. Using this relation, we write the inner and outer angular radii of the ring as θ_{in} and $\theta_{\mathrm{out}} = (1 + f)\theta_{\mathrm{in}}$. The normalized visibility of the ring is given by

$$V_{\mathrm{ring}} = \frac{2}{\pi r_{u\text{-}v}\theta_{\mathrm{in}}(2f + f^2)}$$
$$\times \{(1 + f)J_1[(1 + f)\pi\theta_{\mathrm{in}} r_{u\text{-}v}] - J_1(\pi\theta_{\mathrm{in}} r_{u\text{-}v})\}, \qquad (19)$$

where $r_{u\text{-}v} = (u^2 + v^2)^{1/2}$ is the u-v radius (eq. [2]). The model for the observed visibilities is obtained by using equation (6) with $V_x = V_{\text{ring}}$.

In order to facilitate comparison of our data to puffed-up inner disk models from the literature, we use ring widths derived from radiative transfer modeling by DDN. Specifically, for stars earlier than spectral type B6, we assume $f = 0.27$, and for stars later than B6, we assume $f = 0.18$ (Table 1 from DDN).

3.3.5. Two-Component Model

This model simulates a wide binary, in which visibilities are effectively due to two stationary point sources, with some flux ratio and angular separation vector. We explore flux ratios from 0.2 to 1 and angular separations from 1 to 100 mas. For flux ratios less than 0.2, or angular separations less than 1 mas, the effects of the companions on the visibilities will be negligible, and we can rule out angular separations $\gtrsim 100$ mas from adaptive optics imaging (§ 3.1). The squared visibility for the binary model is

$$V_{\text{binary}}^2 = \frac{1 + R^2 + 2R\cos[(2\pi/\lambda)\boldsymbol{B}\cdot\boldsymbol{s}]}{(1+R)^2} , \qquad (20)$$

where $(\boldsymbol{B}\cdot\boldsymbol{s})/\lambda = \theta(u\sin\psi + v\cos\psi)$, θ is the angular separation of the binary, ψ is the position angle, R is the ratio of the fluxes of the two components, and λ is the observed wavelength.

3.4. Modeling of Individual Sources

For each source, we fitted the PTI and IOTA visibility data with the models described in § 3.3 using grids of parameter values. The grid for face-on disk models was generated by varying θ from 0.01 to 10 mas in increments of 0.01 mas. For inclined disk models, in addition to varying θ, we varied ϕ from 0° to 90° and ψ from 0° to 180°, both in increments of 1°. As mentioned above, $\phi = 0$ corresponds to face-on, and ψ is measured east of north. Since inclined disk models are symmetric under reflections through the origin, we do not explore position angles between 180° and 360°. For the binary model, we varied θ from 1 to 100 mas in increments of 0.01 mas, ψ from 0° to 180° in increments of 1°, and $R = F_2/F_1$ from 0.2 to 1 in increments of 0.001.

For each point in the parameter grid, we generated a model for the observed u-v coverage and calculated the reduced χ^2 (χ_r^2) to determine the "best-fit" model; 1 σ confidence limits were determined by finding the grid points where χ_r^2 equals the minimum value plus one. For inclined disk or binary models, the confidence limits on each parameter were determined by projecting the three-dimensional $\chi_r^2 = \min + 1$ surface onto the one-dimensional parameter spaces.

Tables 4–8 list the best-fit angular size scales (θ) for face-on models, the sizes (θ), position angles (ψ), and inclinations (ϕ) for inclined disk models, and the angular separations (θ), position angles (ψ), and brightness ratios (R) for binary models. Values of χ_r^2 are also included in the tables. Figures 2, 4, 6, 8, and 10 show plots of observed V^2 versus $r_{u\text{-}v}$ for each source along with the curves predicted by various face-on models. Inclined models are not circularly symmetric, and the visibilities are a function of the observed position angle in addition to the projected baseline (Fig. 1). We plot
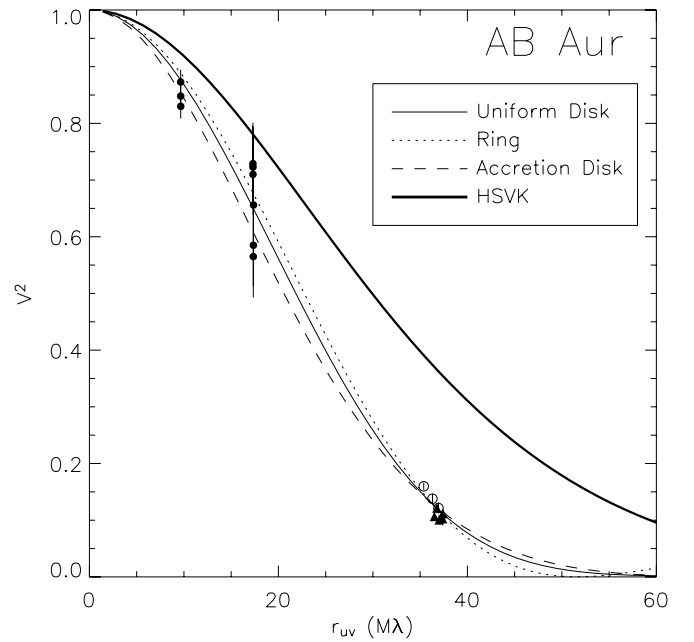

FIG. 2.—V^2 data from IOTA (*filled circles*; MST) and PTI (*other symbols*) for AB Aur, as a function of $r_{u\text{-}v} = (u^2 + v^2)^{1/2}$. PTI data for individual nights are represented by different symbols. Face-on uniform-disk (*thin solid line*), ring (*dotted line*), and accretion disk (*dashed line*) models are overplotted. We also plot the visibilities calculated for an accretion disk model with $R_{\text{in}} = 0.09$ AU and $T_{\text{in}} = 2360$ K (HSVK; *thick solid line*).

the observed and modeled V^2 for inclined models as a function of hour angle in Figures 3, 5, 7, 9, and 11.

The best-fit binary separations for all sources in our sample are $\gtrsim 2.5$ mas. For the distances and approximate masses of the sources in our sample, these separations correspond to orbital periods of many years. Thus, our
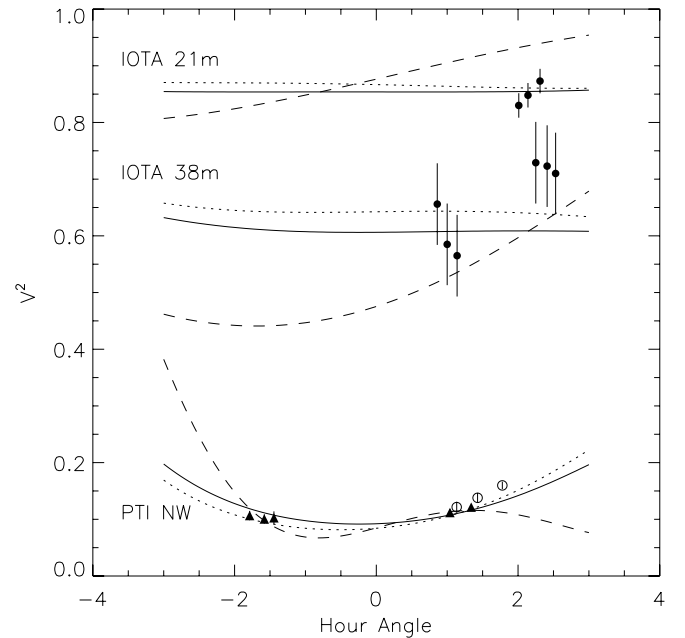

FIG. 3.—PTI and IOTA V^2 data for AB Aur (as in Fig. 2), as a function of hour angle. Overplotted are face-on and inclined accretion disk models (*solid and dotted lines, respectively*), as well as the best-fit binary model (*dashed line*).
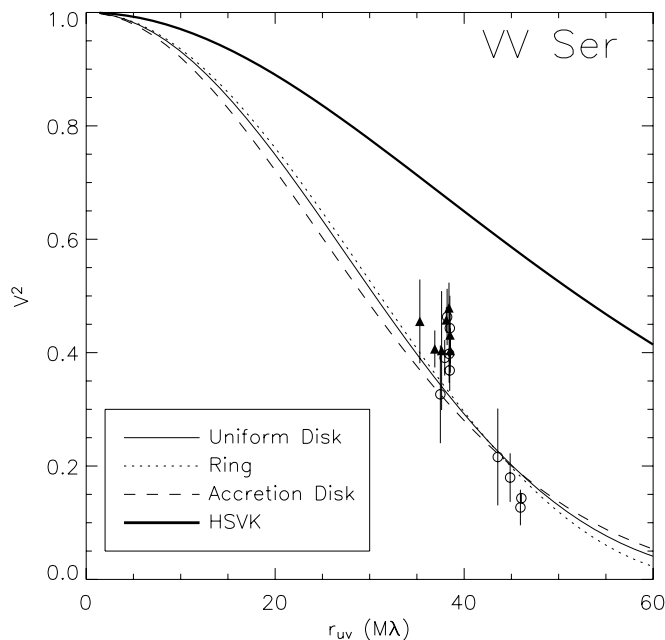
FIG. 4.—PTI V^2 data for VV Ser, as a function of $r_{u-v} = (u^2 + v^2)^{1/2}$. PTI data for individual nights are represented by different symbols. Face-on uniform-disk (*thin solid line*), ring (*dotted line*), and accretion disk (*dashed line*) models are overplotted. We also plot the visibilities calculated for an accretion disk model with $R_{in} = 0.08$ AU and $T_{in} = 2710$ K (HSVK; *thick solid line*).

assumption that the two point sources in the binary model are stationary is justified.

3.4.1. *AB Aur*

The visibilities for AB Aur are consistent with a disklike circumstellar distribution that is inclined by $\lesssim 30°$ (Figs. 2 and 3). From Table 4, the best-fit models indicate size scales[4] between 2.2 and 5.8 mas and an inclination angle between $27°$ and $35°$.

The values of χ_r^2 are significantly lower for inclined models than for face-on models ($\chi^2 \sim 1$ and 2, respectively;

[4] As outlined in §§ 3.3.1–3.3.4, characteristic size scales for different models measure different parts of the brightness distributions: Gaussian models measure FWHM, uniform-disk models measure outer diameters, accretion disk models measure inner disk diameters, and ring models measure inner ring diameters. The spread in quoted angular sizes for a source is mainly due to these differences.

TABLE 4
RESULTS OF MODELING FOR AB AUR

Model	χ_r^2	θ (mas)	ψ (deg)	ϕ[a] (deg)
Face-on Gaussian	2.42	$3.59^{+0.09}_{-0.08}$	...	...
Face-on uniform	1.78	5.34 ± 0.09	...	...
Face-on accretion	1.93	$2.18^{+0.03}_{-0.02}$	...	...
Face-on ring..............	1.92	$3.26^{+0.02}_{-0.03}$	...	...
Inclined Gaussian	0.96	$3.88^{+0.38}_{-0.27}$	103^{+23}_{-25}	35^{+12}_{-18}
Inclined uniform	0.89	$5.80^{+0.65}_{-0.45}$	128^{+30}_{-45}	26^{+10}_{-19}
Inclined accretion.......	0.88	$2.30^{+0.23}_{-0.11}$	105^{+34}_{-45}	27^{+13}_{-17}
Inclined ring..............	0.88	$3.66^{+0.42}_{-0.38}$	144^{+17}_{-51}	28^{+10}_{-18}
Binary model	8.96	$3.41^{+0.13}_{-0.28}$	38^{+7}_{-3}	$0.58^{+0.04}_{-0.03}$

[a] For the binary model, ϕ represents the brightness ratio, $R = F_2/F_1$.

TABLE 5
RESULTS OF MODELING FOR VV SER

Model	χ_r^2	θ (mas)	ψ (deg)	ϕ[a] (deg)
Face-on Gaussian	9.13	2.33 ± 0.09	...	...
Face-on uniform	6.91	3.68 ± 0.12	...	...
Face-on accretion	8.33	1.49 ± 0.05	...	...
Face-on ring..............	5.86	2.30 ± 0.07	...	...
Inclined Gaussian	0.85	$2.56^{+1.66}_{-0.13}$	37^{+6}_{-55}	89^{+1}_{-50}
Inclined uniform	0.85	$3.94^{+2.35}_{-0.17}$	41^{+2}_{-53}	82^{+8}_{-43}
Inclined accretion.......	0.85	$1.62^{+1.58}_{-0.98}$	38^{+5}_{-70}	83^{+7}_{-45}
Inclined ring..............	0.85	$2.44^{+1.92}_{-0.11}$	43^{+5}_{-78}	81^{+9}_{-51}
Binary model	0.85	$8.80^{+1.02}_{-0.95}$	176^{+9}_{-3}	$0.45^{+0.38}_{-0.04}$

[a] For the binary model, ϕ represents the brightness ratio, $R = F_2/F_1$.

Table 4), and the data cannot be well fitted by a binary model ($\chi_r^2 \sim 8$).

3.4.2. *VV Ser*

The angular size scales for best-fit disk models range from 1.5 to 3.9, and the disk inclinations are between $80°$ and $90°$ (Table 5). An inclined disk model clearly fits the VV Ser data better than a face-on model (Figs. 4 and 5). Inclined model fits give $\chi_r^2 < 1$, while face-on model fits have $\chi_r^2 > 5$ (Table 5). However, as indicated in Figure 1, the u-v coverage for this object is rather sparse and precludes placing stringent constraints on the value of ϕ. Moreover, with such sparse u-v coverage, a binary model cannot be ruled out (Fig. 5).

3.4.3. *V1685 Cyg*

The size scales for V1685 Cyg under the assumptions of various disk models range from 1.3 to 3.9 mas, and the inclinations are between $49°$ and $51°$ (Table 6). The visibility
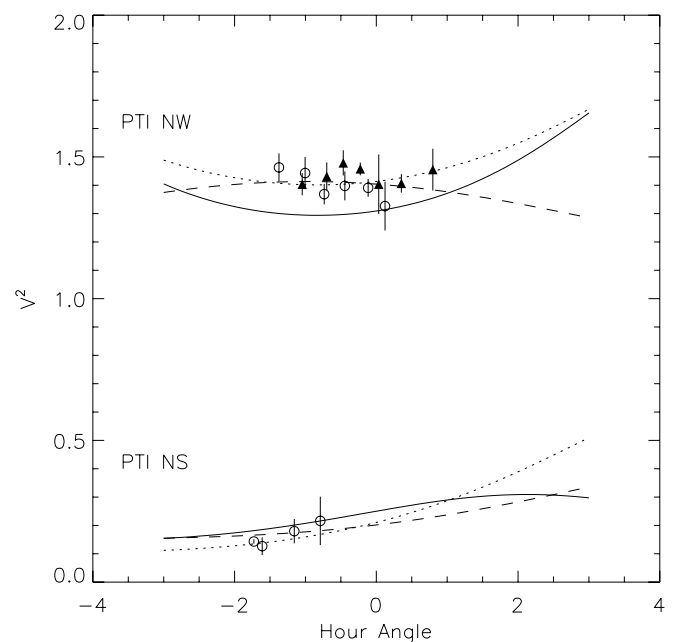

FIG. 5.—PTI V^2 data for VV Ser (as in Fig. 4), as a function of hour angle. For clarity, we have plotted $V^2 + 1$ for the data taken with the northwest baseline. Overplotted are face-on and inclined accretion disk models (*solid and dotted lines, respectively*), as well as the best-fit binary model (*dashed line*).
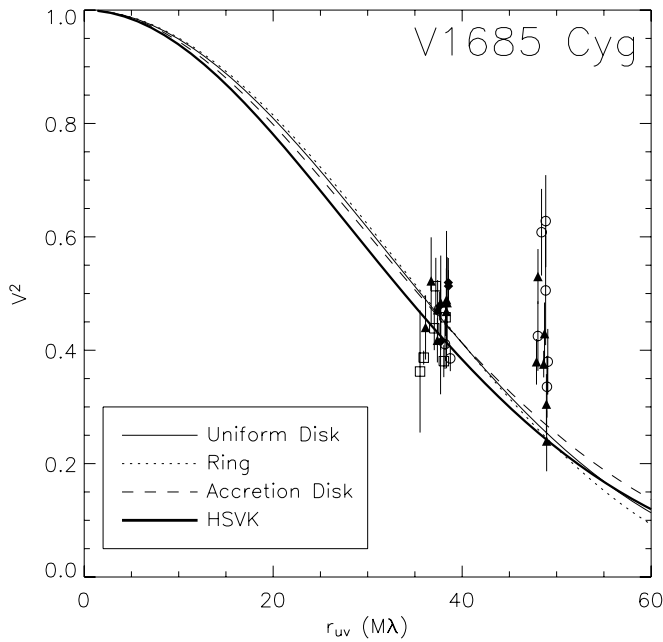
FIG. 6.—PTI V^2 data for V1685 Cyg, as a function of $r_{u\text{-}v} = (u^2 + v^2)^{1/2}$. PTI data for individual nights are represented by different symbols. Face-on uniform-disk (*thin solid line*), ring (*dotted line*), and accretion disk (*dashed line*) models are overplotted. We also plot the visibilities calculated for an accretion disk model with $R_{\rm in} = 0.63$ AU and $T_{\rm in} = 2060$ K (HSVK; *thick solid line*).

data are not fitted very well by any model, although of those considered, inclined disks fit best (Figs. 6 and 7). While we cannot rule out a binary model, we note that $\chi_r^2 \sim 3$ for the binary model, compared to $\chi_r^2 \sim 2$ for inclined disk models (Table 6).

Better coverage of the u-v plane should help to improve our understanding of this source (Fig. 1).

3.4.4. AS 442

The PTI data for AS 442 generally have low signal-to-noise ratios, and it is difficult to distinguish between different models. Nevertheless, we can make an approximate determination of the size scale, although we cannot distinguish between inclined disk, face-on disk, or binary models (Figs. 8 and 9). The size scales for various disk models range from 0.9 to 2.7 mas (Table 7).

TABLE 6
RESULTS OF MODELING FOR V1685 CYG

Model	χ_r^2	θ (mas)	ψ (deg)	ϕ^{a} (deg)
Face-on Gaussian	6.51	1.96 ± 0.11	...	...
Face-on uniform	7.52	$3.17^{+0.16}_{-0.15}$	...	...
Face-on accretion	6.75	1.27 ± 0.06	...	...
Face-on ring..............	8.10	1.92 ± 0.09	...	...
Inclined Gaussian	2.32	$2.43^{+0.44}_{-0.37}$	125^{+9}_{-28}	51^{+12}_{-16}
Inclined uniform	2.36	$3.91^{+0.60}_{-0.55}$	124^{+9}_{-24}	50^{+11}_{-14}
Inclined accretion.......	2.33	$1.57^{+0.27}_{-0.22}$	124^{+9}_{-22}	50^{+12}_{-14}
Inclined ring..............	2.38	$2.33^{+0.37}_{-0.29}$	122^{+10}_{-24}	49^{+11}_{-13}
Binary model	3.33	$3.41^{+0.37}_{-0.56}$	62^{+6}_{-11}	$0.24^{+0.08}_{-0.04}$

^{a} For the binary model, ϕ represents the brightness ratio, $R = F_2/F_1$.

3.4.5. MWC 1080

The PTI and IOTA observations for MWC 1080 are completely incompatible with face-on models ($\chi_r^2 > 40$), and significantly nonzero inclinations are required to fit the data well (Figs. 10 and 11).

The best-fit inclination angles for various disk models range from $51°$ to $56°$, and the angular size scales are between 1.5 and 4.1 mas (Table 8). For this source, we can rule out a binary model with a relatively high degree of confidence: $\chi_r^2 \sim 10$ for the binary model, compared to $\chi_r^2 \sim 2$ for inclined disk models.

4. DISCUSSION

As discussed in § 1, there is currently a wide variety of evidence that supports the existence of circumstellar disks around many HAEBE stars. Our new PTI results strengthen this contention. Resolved, small-scale (~ 1 AU) distributions of dust are found in all observed sources, and the nonsymmetric intensity distributions of best-fit models for most objects provide support for inclined disk geometries.

We suggest that the material around VV Ser, V1685 Cyg, and MWC 1080 is significantly inclined, and we cannot rule out a high inclination angle for AS 442. This hypothesis is compatible with observed optical variability in VV Ser and AS 442 ($\Delta V_{\rm VV\,Ser} \sim 2$, $\Delta V_{\rm AS\,442} \sim 1$; Herbst & Shevchenko 1999), which has been attributed to variable obscuration from clumps of dust orbiting in inclined circumstellar disks.

The AB Aur data, in contrast, are consistent with a circumstellar distribution that is within $35°$ of face-on. This agrees well with MST and is compatible with modeling of scattered light observed with the *Hubble Space Telescope*, which suggests an inclination angle $\lesssim 45°$ (Grady et al. 1999). The small amplitude of variability in AB Aur
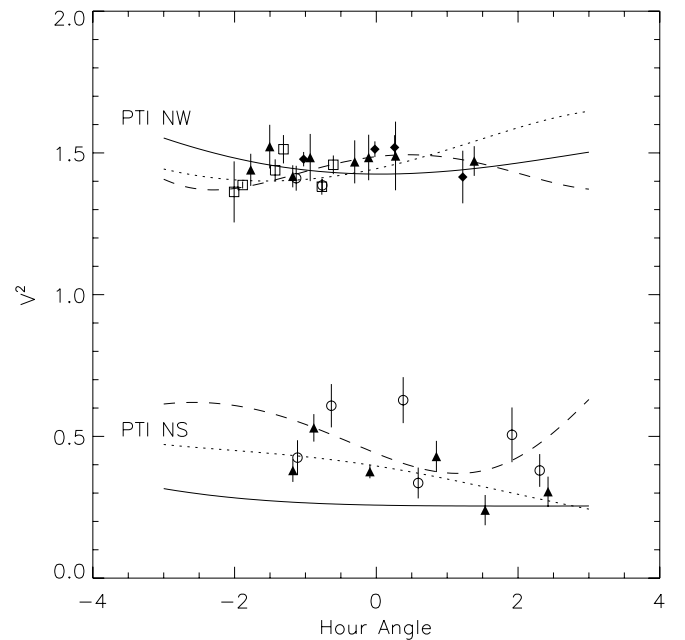

FIG. 7.—PTI V^2 data for V1685 Cyg (as in Fig. 6), as a function of hour angle. For clarity, we have plotted $V^2 + 1$ for the data taken with the northwest baseline. Overplotted are face-on and inclined accretion disk models (*solid and dotted lines, respectively*), as well as the best-fit binary model (*dashed line*).
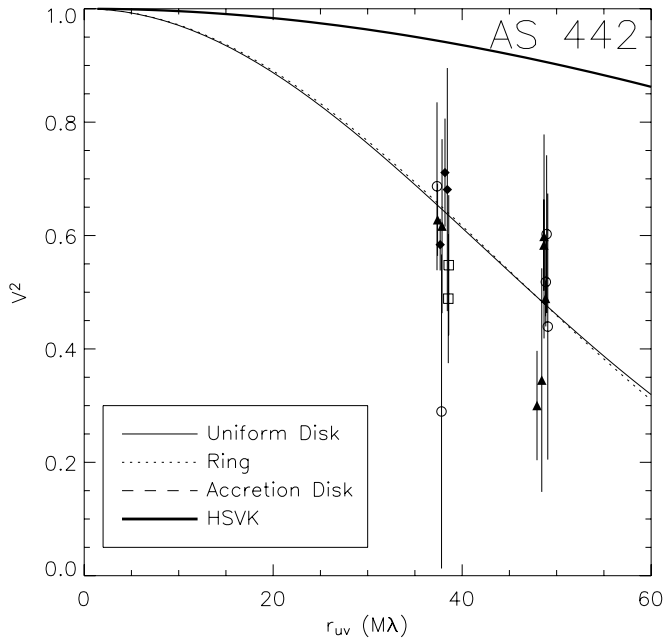
FIG. 8.—PTI V^2 data for AS 442, as a function of $r_{u\text{-}v} = (u^2 + v^2)^{1/2}$. PTI data for individual nights are represented by different symbols. Face-on uniform-disk (*thin solid line*), ring (*dotted line*), and accretion disk (*dashed line*) models are overplotted. We also plot the visibilities calculated for an accretion disk model with $R_{in} = 0.10$ AU and $T_{in} = 2000$ K (HSVK; *thick solid line*).

TABLE 7
RESULTS OF MODELING FOR AS 442

Model	χ_r^2	θ (mas)	ψ (deg)	ϕ[a] (deg)
Face-on Gaussian	0.99	1.49 ± 0.19	...	...
Face-on uniform	1.04	$2.44^{+0.29}_{-0.28}$	...	...
Face-on accretion	0.99	$0.95^{+0.13}_{-0.12}$	...	...
Face-on ring..............	1.07	1.55 ± 0.17	...	...
Inclined Gaussian	0.94	$1.63^{+0.82}_{-0.29}$	60^{+120}_{-60}	41^{+49}_{-41}
Inclined uniform	0.94	$2.67^{+1.29}_{-0.34}$	63^{+117}_{-63}	39^{+51}_{-39}
Inclined accretion.......	0.94	$1.03^{+0.57}_{-0.18}$	63^{+117}_{-63}	36^{+54}_{-36}
Inclined ring..............	0.95	$1.70^{+0.80}_{-0.28}$	65^{+115}_{-65}	38^{+52}_{-38}
Binary model	0.95	$2.69^{+0.69}_{-1.50}$	30^{+32}_{-19}	$0.21^{+0.79}_{-0.01}$

[a] For the binary model, ϕ represents the brightness ratio, $R = F_2/F_1$.

inclined accretion disk models, respectively (§ 3.3.3), and $R_{\dot{M}=0}$ and $R_{\dot{M}\neq 0}$ are the radii calculated using the HSVK flat disk models without accretion and with accretion effects included, respectively. No estimate of $\dot{M}$ is available fo AS 442.

Our data for the later-type stars AB Aur, VV Ser, and AS 442 are fairly consistent with the puffed-up inner disk models of DDN, assuming inner disk temperatures $\gtrsim 2000$ K. In contrast, puffed-up inner disk models are completely incompatible with the PTI results for the very early-type stars in our sample, V1685 Cyg and MWC 1080. The radius of the inner wall, R_{in}, predicted by DDN is

$$R_{in} = \sqrt{\frac{L_*}{4\pi T_{in}^4 \sigma}(1 + f)}, \qquad (21)$$

where L_* is the (published) stellar luminosity, T_{in} is the temperature of the inner wall, and f is the ratio of the width of

($\Delta V \sim 0.25$; Herbst & Shevchenko 1999) is also consistent with this low inclination angle (under the assumption that variability is caused by time-dependent circumstellar obscuration).

The low inclination angle does *not*, however, agree with millimeter-wavelength imaging in the ^{13}CO (1–0) line, which yields an estimated inclination of 76° for the AB Aur disk (Mannings & Sargent 1997).

The angular sizes determined from our observations are generally in good agreement with the noninclined ($\phi = 0$) flat accretion disk models of HSVK for early-type Herbig Be stars, V1685 Cyg and MWC 1080, but not for the later-type stars, AB Aur, VV Ser, and AS 442 (the spectral type for VV Ser, A0, is uncertain by ± 5 spectral subclasses; Mora et al. 2001). Angular sizes derived from the earlier IOTA observations (MST) were often an order of magnitude larger than those predicted by the HSVK models, and on this basis MST ruled these models out.

HSVK determined the best-fit models for the SEDs of HAEBE sources by assuming a face-on disk geometry, adjusting the accretion rate to match the mid-IR flux, and then adjusting the size of the inner hole to match the near-IR flux. We compare our results with theirs in a qualitative way by plotting the visibilities predicted by the HSVK models along with the observed PTI and IOTA visibilities in Figures 2, 4, 6, 8, and 10. For a more quantitative comparison, we use published luminosities, effective temperatures, and accretion rates (HSVK) to calculate the inner radii predicted by flat accretion disk models with $T_{in} = 2000$ K (eqs. [13] and [14]) and compare these estimates to our interferometric results (which were also derived assuming $T_{in} = 2000$ K; § 3.3.3).

In Table 9, $R_{\text{face-on}}$ and R_{inclined} are the inner radii determined by fitting the interferometric data to face-on and
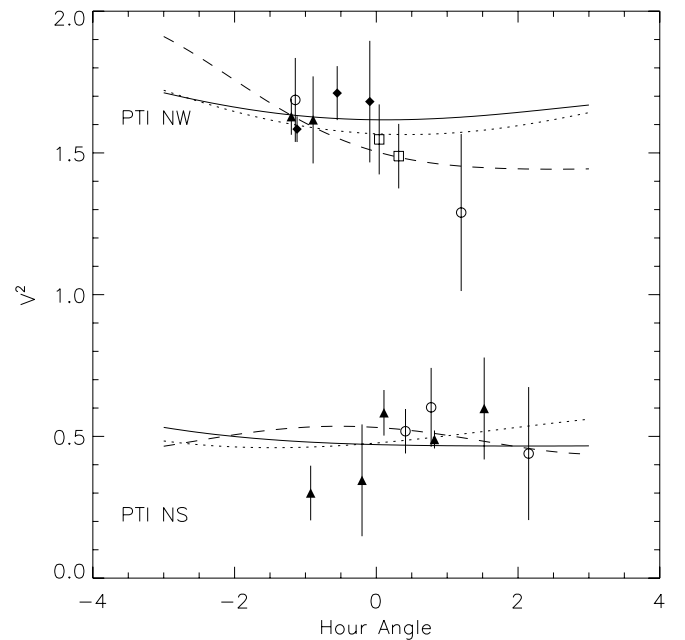

FIG. 9.—PTI V^2 data for AS 442 (as in Fig. 8), as a function of hour angle. For clarity, we have plotted $V^2 + 1$ for the data taken with the northwest baseline. Overplotted are face-on and inclined accretion disk models (*solid and dotted lines, respectively*), as well as the best-fit binary model (*dashed line*).
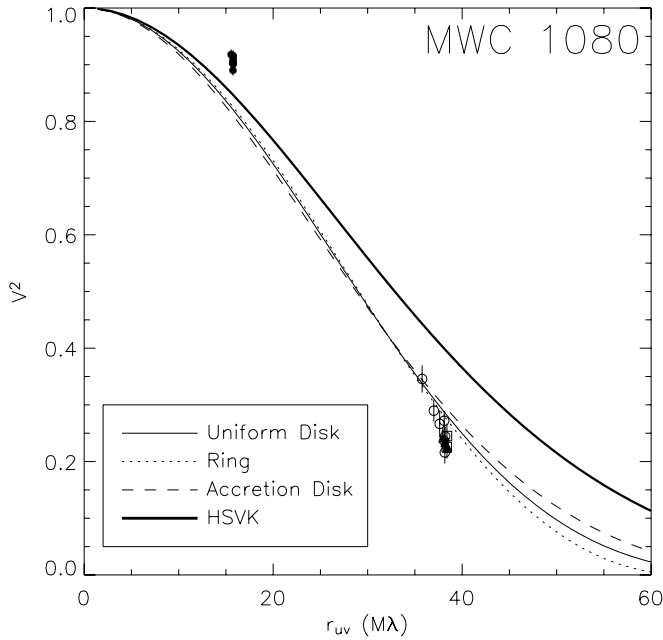
Fig. 10.—V^2 data from PTI (*symbols*) and IOTA (*filled circles*; MST) for MWC 1080, as a function of $r_{u-v} = (u^2 + v^2)^{1/2}$. PTI data for individual nights are represented by different symbols. Face-on uniform-disk (*thin solid line*), ring (*dotted line*), and accretion disk (*dashed line*) models are overplotted. We also plot the visibilities calculated for an accretion disk model with $R_{in} = 0.59$ AU and $T_{in} = 2490$ K (HSVK; *thick solid line*). While none of these face-on models fit the data well, good fits are obtained with inclined models (Fig. 11).

the inner wall to its radius. Based on DDN, we assume $f = 0.27$ for stars earlier than spectral type B6 and $f = 0.18$ for later-type stars. We calculate R_{in} for $T_{in} = 1500$ and 2000 K (likely sublimation temperatures for silicate and graphite dust grains, respectively) and compare these to the ring diameters derived from fitting to near-IR interferometric visibilities. In Table 10, $R_{face-on}$ and $R_{inclined}$ represent the inner radii determined for face-on and inclined ring models, respectively (§ 3.3.4), and R_{2000} and R_{1500} are the inner radii predicted by the DDN puffed-up inner disk models, assuming sublimation temperatures of 2000 and 1500 K, respectively.

We note that the comparison of our interferometric results to physical models should be independent of the assumed distance (see the Appendix). The inner radius is $\propto L^{1/2} \propto d$ in both the DDN and HSVK models, and the

TABLE 8
RESULTS OF MODELING FOR MWC 1080

Model	χ_r^2	θ (mas)	ψ (deg)	ϕ[a] (deg)
Face-on Gaussian	56.33	2.34 ± 0.05	...	...
Face-on uniform	42.04	3.84 ± 0.07	...	...
Face-on accretion	54.24	1.54 ± 0.03	...	...
Face-on ring..............	36.00	$2.33^{+0.04}_{-0.05}$	...	...
Inclined Gaussian	3.21	$2.61^{+0.11}_{-0.08}$	71^{+11}_{-9}	56^{+6}_{-5}
Inclined uniform	2.54	$4.13^{+0.12}_{-0.10}$	70^{+10}_{-8}	53^{+7}_{-5}
Inclined accretion......	3.07	$1.69^{+0.07}_{-0.05}$	71^{+10}_{-9}	55^{+5}_{-3}
Inclined ring..............	2.28	2.47 ± 0.06	69^{+10}_{-9}	51 ± 6
Binary model	9.32	$2.57^{+0.22}_{-0.18}$	56^{+4}_{-3}	0.36 ± 0.02

[a] For the binary model, ϕ represents the brightness ratio, $R = F_2/F_1$.

TABLE 9
COMPARISON WITH HSVK MODELS

Source	$R_{face-on}$[a] (AU)	$R_{inclined}$[a] (AU)	$R_{\dot{M}=0}$ (AU)	$R_{\dot{M}\neq0}$ (AU)
AB Aur	0.15 ± 0.01	0.16 ± 0.01	0.07	0.12
VV Ser	0.23 ± 0.01	0.25 ± 0.19	0.03	0.13
V1685 Cyg	0.64 ± 0.03	0.79 ± 0.13	0.44	0.71
AS 442	0.29 ± 0.04	0.31 ± 0.12	0.10	...
MWC 1080	0.77 ± 0.02	0.85 ± 0.03	0.79	0.79

[a] Error bars based on 1 σ uncertainties of best-fit face-on and inclined accretion disk models.

linear sizes determined from our interferometric results (converted from modeled angular sizes) are also $\propto d$, and thus, the comparison is independent of d.

Flat accretion disk models HSVK are generally in good agreement with the observed visibility data for early-type B stars, while puffed-up inner disk models (DDN) seem more consistent for later-type stars. We speculate that this could be due to different accretion mechanisms in earlier- and later-type stars. A similar idea has been put forward based on the results of Hα spectropolarimetry, where differences in the observations for early-type HBe stars and later-type HAe stars have been attributed to a transition from disk accretion in higher mass stars to magnetic accretion in lower mass stars (Vink et al. 2002).

There is always the possibility that the visibilities for some of the observed HAEBE sources may be (partially) due to close companions. For AB Aur and MWC 1080, we can rule out binary models (with separations $\gtrsim 1$ mas) with a high degree of confidence. However, MWC 1080 is an eclipsing binary with a period of $P \approx 2.9$ days (Shevchenko et al. 1994; Corporon & Lagrange 1999). The separation is much
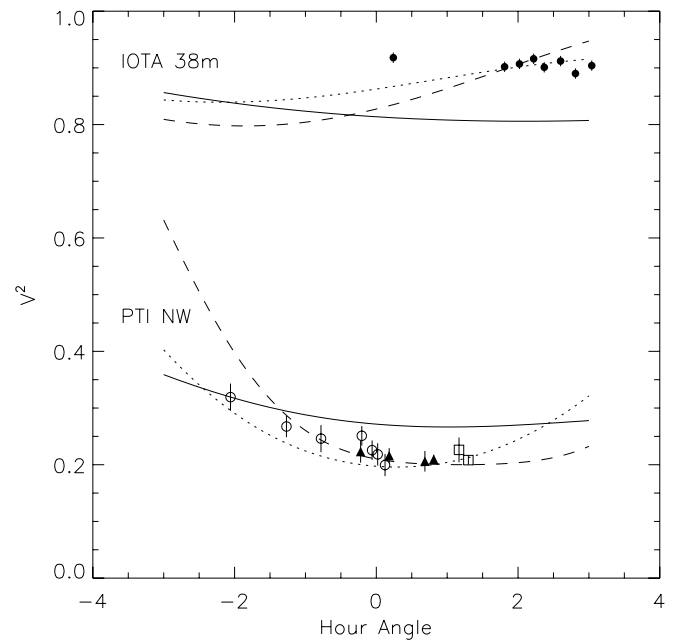

Fig. 11.—PTI and IOTA V^2 data for MWC 1080 (as in Fig. 10), as a function of hour angle. Overplotted are face-on and inclined accretion disk models (*solid and dotted lines, respectively*), as well as the best-fit binary model (*dashed line*). Note the significant improvement in the fit when inclination effects are included in the model.

TABLE 10
COMPARISON WITH DDN MODELS

Source	$R_{\text{face-on}}$[a] (AU)	R_{inclined}[a] (AU)	R_{2000} (AU)	R_{1500} (AU)
AB Aur	0.23 ± 0.01	0.26 ± 0.03	0.32	0.57
VV Ser	0.36 ± 0.01	0.38 ± 0.14	0.24	0.42
V1685 Cyg	0.96 ± 0.05	1.17 ± 0.16	3.71	6.59
AS 442	0.47 ± 0.05	0.56 ± 0.13	0.52	0.93
MWC 1080	1.17 ± 0.02	1.24 ± 0.03	8.69	15.45

[a] Error bars based on 1 σ uncertainties of best-fit face-on and inclined ring models.

too small to be detected by PTI, and the observed visibilities for this source are thus probably due to an inclined *circumbinary* disk. Observations over a time span of $\sim$100 days (Table 2), with visibilities that are fairly constant in time (Figs. 6 and 7), provide some evidence against V1685 Cyg being a binary. As yet, the binarity status of AS 442 and VV Ser remains uncertain based on our visibility data, although radial velocity variations of spectral lines in AS 442 have been attributed to a binary with $P \approx 64$ days and $e \approx 0.2$ (Corporon & Lagrange 1999).

5. SUMMARY

We observed the HAEBE sources AB Aur, VV Ser, V1685 Cyg (BD $+40°4124$), AS 442, and MWC 1080 at 2.2 μm with the Palomar Testbed Interferometer. These are only the second published near-IR interferometric observations of HAEBE stars. From these high angular resolution data, we determined the angular size scales and orientations predicted by uniform-disk, Gaussian, ring, and accretion disk models, and we examined whether the data were consis-

tent with binary models. AB Aur appears to be surrounded by a disk that is inclined by $\lesssim 30°$, while VV Ser, V1685 Cyg, and MWC 1080 are associated with more highly inclined circumstellar disks. With the available data, we cannot distinguish between different radial distributions, such as Gaussians, uniform disks, rings, or accretion disks.

While the angular size scales determined in this work are generally consistent with the only other near-IR interferometric measurements of HAEBE stars by MST, our measurements are the first that show evidence for significantly inclined morphologies. Moreover, the derived angular sizes for early-type Herbig Be stars in our sample, V1685 Cyg and MWC 1080, agree fairly well with those predicted by face-on accretion disk models used by HSVK to explain observed spectral energy distributions. The observations of AB Aur, VV Ser, and AS 442 are, however, not entirely compatible with these models and may be better explained through the puffed-up inner disk models of DDN.

APPENDIX

DISTANCE ESTIMATES

AB Aur is associated with the Taurus-Auriga molecular cloud, and thus the estimated distance to this source ($d = 140$ pc) is accurate to $\sim$10%. Photometric studies of VV Ser and other stars in Serpens estimated distances of $d \approx 250$ pc (Chavarría-K et al. 1988) and $d \approx 310$ pc (de Lara, Chavarría-K, & López-Molina 1991), while an earlier study based on photometry of a single source estimated $d = 440$ pc (Strom, Grasdalen, & Strom 1974). Based on these estimates, we adopt a distance of 310 pc. Distance estimates to V1685 Cyg range from 980 pc (based on an extinction-distance diagram for 132 stars within 3°5; Shevchenko, Ibragimov, & Chernysheva 1991), to 1000 pc (based on locating V1685 Cyg on the main sequence; Strom et al. 1972), to 2200 pc (based on photometry of stars in a large-scale region around V1685 Cyg; Hiltner & Johnson 1956). We adopt a distance of $d = 1000$ pc to V1685 Cyg, since the 2200 pc estimate would imply a luminosity higher than expected for the published spectral type. AS 442 is associated with the North American Nebula, and thus the adopted distance of 600 pc is probably accurate to $\sim$10%. The distance to MWC 1080 has been determined by fitting photometric observations to the main sequence ($d = 1000$ pc; HSVK) and using the Galactic rotation curve ($d = 2500$ pc; Cantó et al. 1984). We adopt a distance of 1000 pc to MWC 1080, since the 2500 pc estimate based on the Galactic rotation curve would imply a luminosity much higher than expected for the published spectral type. Moreover, the 2500 pc estimate is uncertain by $\sim$50%, while the 1000 pc estimate is accurate to $\sim$20%.

REFERENCES

Bigay, J. H., & Garnier, R. 1970, A&AS, 1, 15
Boden, A. F., Colavita, M. M., van Belle, G. T., & Shao, M. 1998, Proc. SPIE, 3350, 872
Born, M., & Wolf, E. 1999, Principles of Optics (7th ed.; Cambridge: Cambridge Univ. Press)
Cantó, J., Rodríguez, L. F., Calvet, N., & Levreault, R. M. 1984, ApJ, 282, 631
Chavarría-K, C., de Lara, E., Finkenzeller, U., Mendoza, E. E., & Ocegueda, J. 1988, A&A, 197, 151

Chiang, E. I., & Goldreich, P. 1997, ApJ, 490, 368
Colavita, M. M. 1999, PASP, 111, 111
Colavita, M. M., et al. 1999, ApJ, 510, 505
Corcoran, M., & Ray, T. P. 1997, A&A, 321, 189
Corporon, P. 1998, Ph.D. thesis, Univ. Joseph Fourier de Grenoble
Corporon, P., & Lagrange, A.-M. 1999, A&AS, 136, 429
de Lara, E., Chavarría-K, C., & López-Molina, G. 1991, A&A, 243, 139
Dullemond, C. P., Dominik, C., & Natta, A. 2001, ApJ, 560, 957 (DDN)

Eiroa, C., et al. 2002, A&A, 384, 1038
Grady, C. A., Woodgate, B., Bruhweiler, F. C., Boggess, A., Plait, P., Lindler, D. L., Clampin, M., & Kalas, P. 1999, ApJ, 523, L151
Hartmann, L., Kenyon, S. J., & Calvet, N. 1993, ApJ, 407, 219
Herbig, G. H. 1960, ApJS, 4, 337
Herbst, W., & Shevchenko, V. S. 1999, AJ, 118, 1043
Hillenbrand, L. A., Strom, S. E., Vrba, F. J., & Keene, J. 1992, ApJ, 397, 613 (HSVK)
Hiltner, W. A., & Johnson, H. L. 1956, ApJS, 2, 389
Lynden-Bell, D., & Pringle, J. E. 1974, MNRAS, 168, 603
Mannings, V. 1994, MNRAS, 271, 587
Mannings, V., Koerner, D. W., & Sargent, A. I. 1997, Nature, 388, 555
Mannings, V., & Sargent, A. I. 1997, ApJ, 490, 792
———. 2000, ApJ, 529, 391
Meeus, G., Waters, L. B. F. M., Bouwman, J., van den Ancker, M. E., Waelkens, C., & Malfait, K. 2001, A&A, 365, 476
Millan-Gabet, R., Schloerb, F. P., & Traub, W. A. 2001, ApJ, 546, 358 (MST)
Millan-Gabet, R., Schloerb, F. P., Traub, W. A., Malbet, F., Berger, J. P., & Bregman, J. D. 1999, ApJ, 513, L131
Miroshnichenko, A., Ivezić, Ž., Vinković, D., & Elitzur, M. 1999, ApJ, 520, L115
Mora, A., et al. 2001, A&A, 378, 116

Natta, A., Grinin, V. P., & Mannings, V. 2000, in Protostars and Planets IV, ed. V. Mannings, A. Boss, & S. S. Russell (Tucson: Univ. Arizona Press), 559
Natta, A., Palla, F., Butner, H. M., Evans, N. J., II, & Harvey, P. M. 1993, ApJ, 406, 674
Natta, A., Prusti, T., Neri, R., Wooden, D., Grinin, V. P., & Mannings, V. 2001, A&A, 371, 186
Oudmaijer, R. D., et al. 2001, A&A, 379, 564
Piétu, V., Dutrey, A., & Kahane, C. 2003, A&A, 398, 565
Shevchenko, V. S., Grankin, N., Ibragimov, M. B., Kondratiev, V. Y., & Melnikov, S. 1994, in ASP Conf. Ser. 62, The Nature and Evolutionary Status of Herbig Ae/Be Stars, ed. P. S. Thé, M. R. Pérez, & E. P. J. van den Heuvel (San Francisco: ASP), 43
Shevchenko, V. S., Ibragimov, M. A., & Chernysheva, T. L. 1991, Soviet Astron., 35, 229
Skrutskie, M. F., Meyer, M. R., Whalen, D., & Hamilton, C. 1996, AJ, 112, 2168
Steenman, H., & Thé, P. S. 1991, Ap&SS, 184, 9
Strom, K. M., Strom, S. E., Breger, M., Brooke, A. L., Yost, J., Grasdalen, G. L., & Carrasco, L. 1972, ApJ, 173, L65
Strom, S. E., Grasdalen, G. L., & Strom, K. M. 1974, ApJ, 191, 111
Vink, J. S., Drew, J. E., Harries, T. J., & Oudmaijer, R. D. 2002, MNRAS, 337, 356